Simultaneous Interfacial Reactivity and Topography Mapping with Scanning Ion Conductance Microscopy (SICM)

Dmitry Momotenko, Kim McKelvey†, Minkyung Kang, Gabriel N. Meloni and Patrick R. Unwin**

Department of Chemistry, University of Warwick, Coventry, CV4 7AL, United Kingdom

†Present address: Department of Chemistry, University of Utah, 315 S. 1400 E., Salt Lake City, UT 84112, United States

*p.r.unwin@warwick.ac.uk

*d.momotenko@warwick.ac.uk

ABSTRACT Scanning ion conductance microscopy (SICM) is a powerful technique for imaging the topography of a wide range of materials and interfaces. In this report we develop the use and scope of SICM, showing how it can be used for mapping spatial distributions of ionic fluxes due to (electro)chemical reactions occurring at interfaces. The basic idea is that there is a change of ion conductance inside a nanopipette probe when it approaches an active site, where the ionic composition is different to that in bulk solution, and this can be sensed via the current flow in the nanopipette with an applied bias. Careful tuning of the tip potential allows the current response to be sensitive to either topography or activity, if desired. Furthermore, the use of a distance modulation SICM scheme allows reasonably faithful probe positioning using the resulting AC response, irrespective of whether there is a reaction at the interface that changes the local ionic composition. Both strategies (distance modulation or tuned bias) allow simultaneous topography-activity mapping with a single channel probe. The application of SICM reaction imaging is demonstrated on several examples, including voltammetric mapping of electrocatalytic reactions on electrodes and high-speed electrochemical imaging at rates approaching 4 s per image frame. These two distinct approaches provide movies of electrochemical current as a function of potential with hundreds of frames (images) of surface reactivity, to reveal a wealth of spatially-resolved information on potential (and time) – dependent electrochemical phenomena. The experimental studies are supported by detailed finite element method modeling that places the technique on a quantitative footing.

KEYWORDS Scanning ion conductance microscopy, high-speed scanning, electrochemical imaging, nanopipette

INTRODUCTION

Since its invention by Hansma *et al*.,[1] scanning ion conductance microscopy (SICM) has developed into a powerful scanning electrochemical probe microscopy (SEPM) for non-contact nanoscale visualization of surface topography, finding application in imaging living cells[2-6] and cell membranes (down to the single protein level)[7], and as a complementary technique for accurate probe-to-substrate distance control, when combined with other scanning probe routines.[8-13] In essence, the operation of SICM is based on the detection of changes of the conductance current, flowing between two quasi-reference counter electrodes (QRCEs), one in a nanopipette filled with electrolyte and one in the bulk solution. The current magnitude is a measure of resistance of the pipette probe and the tip-to-substrate gap. This two-electrode cell arrangement is typically built on relatively straightforward and inexpensive instrumentation. Similar to other electrochemical nanopipette techniques,[14-18] simple probe design, along with high reproducibility and low cost of tip fabrication (nanopipettes are produced by pulling glass or quartz capillaries to a sharp point with a laser puller) and easily tunable probe size (from a few microns in diameter down to a level of a few nanometers). That provides SICM with high resolving power and considerable flexibility of applications.

Although SICM has mainly been concerned with topographical imaging, it is increasingly recognized that the technique has wider scope and applications.[19-21] SICM is a sensitive tool for the detection of local ion fluxes,[22] but unlike some other electrochemical methods, does not require the analyte species to be electroactive, since the probe monitors conductivity changes in the confined region between the sample and the pipette opening. Thus, SICM has been used to study individual pores and ion channels in artificial and living cell membranes.[23-27] Measurements of ion flux through the pipette orifice can be also used to explore ion current

rectification phenomena[28,29] at interfaces[30,31] opening up exciting opportunities to map spatial distributions of surface charge and to probe heterogeneous acid-base equilibria.[20,21]

In this work we introduce new functional capabilities of ion conductance microscopy demonstrating its potential for imaging spatially distributed (electro)chemical reactions through the detection of ionic fluxes near active sites. We provide proof-of-concept applications of this technique for dynamic imaging of electrochemical reactions at electrodes, first by recording the ion conductance response to a series of voltammetric sweeps, over wide potential range, with the pipette at a set of coordinates (image pixels) to map out oxidation and reduction reactions occurring at the electrode. Second, we demonstrate the potential of SICM for high-speed visualization of electroactivity at rates approaching 4 s per image frame.

We highlight herein a number of advantages of SICM compared to other electrochemical probe imaging techniques (such as scanning electrochemical microscopy, SECM).[32] First, is the possibility of mapping topography and reactivity simultaneously in exactly same location (unlike double-barrel combined SECM-SICM probes)[10,33] and without need for special apparatus as required, for example, for shear force-SECM,[34] SECM-atomic force microscopy (AFM)[35,36] and intermittent contact-SECM.[37] SECM alone has the issue that topography and activity are not easily separated. Second, SICM is characterized by very simple probe fabrication (a few seconds to pull nanopipette probes with a laser puller, with no need for additional microfabrication facilities or laborious operations for electrode preparation) and probe handling (nanoscale amperometric SECM tips are very vulnerable to damage from electrostatic discharge and/or etching of the electrode material).[38] Third, SICM probes are much less likely to suffer from contamination effects, in contrast to nanoelectrodes, where a metal or carbon surface must maintain high activity for large periods. A strength of the technique we describe is that it is

quantitative, and we provide theoretical support for the experimental observations by comparison of experimental data with finite element modeling. Since all electrochemical reactions are accompanied by changes in local ionic composition (speciation), a fact that is also true for many other interfacial chemical reactions, the studies herein provide a foundation for SICM to become a powerful general probe of local interfacial reactivity.

EXPERIMENTAL

Chemicals

Ferrocene methanol ($FcCH_2OH$, ≥ 97 %, Sigma-Aldrich), hydrazine sulfate (≥99.0%, Sigma-Aldrich) and KNO_3 (≥ 99.0 %, Sigma-Aldrich) were used as received. Deionized (DI) water produced by Purite Select HP with resistivity 18.2 MΩ cm (25 °C) was used to prepare aqueous solutions. Ferrocenylmethyl trimethylammonium hexafluorophosphate ($FcTMA^+$) was synthesized in house as described elsewhere.[39]

Nanopipette probes

Nanopipettes with tip radii of approximately 95 nm and 200 nm were pulled from single-barrel borosilicate glass capillaries containing a filament (GC120F-10, Harvard Apparatus) using a laser pipette puller (P-2000, Sutter Instruments). For geometric characterization, nanopipettes were gold-coated and visualized using a field-emission scanning electron microscope (FE-SEM, Zeiss SUPRA 55 VP). Nanoscale characterization of the geometry of uncoated nanopipette tips was carried out using a transmission electron microscope (TEM) JEOL 2000FX at 200 kV accelerating voltage.

Scanning ion conductance microscopy (SICM) setup

Pipette probes were mounted on a custom made probe holder and coarsely positioned over a sample with a mechanical micropositioner (Newport, M-461-XYZ-M) and the aid of a 3MP digital camera (PixeLink PL-B776U) with 4X magnification lens. The electrolyte solution in the nanopipette probes contained no redox species, while the bulk solution was composed of both supporting electrolyte salt and redox mediator. Precise control and translation of the probe in the vertical direction (normal to the electrode surface of interest) was achieved with a single axis nanopositioner (Physik Instrumente, P-753.3CD). A small vertical oscillation of the probe (40 nm peak-to-peak) at typical frequencies of 270 – 370 Hz was applied using a lock-in amplifier (Stanford Research Systems, SR830) to induce an alternating current (AC), the magnitude of which served as a positional feedback (distance-modulated SICM).[40,41] Scanning was accomplished with a high-precision XY nanopositioning piezoelectric stage (MadCityLabs, Nano-Bio300) or high-dynamics nanopositioner (Physik Instrumente, model P-733.2DD) for high-speed imaging. The piezoelectric positioners were mounted inside a faraday cage, built on an optical table (Newport, RS 2000) to avoid mechanical vibrations, which incorporated acoustic insulation, vacuum insulating panels (Kevothermal) and aluminium heat sinks (aimed at reducing thermal fluctuations and drift of the piezoelectric positioners[42]). Electrochemical measurements were performed with a custom-built bipotentiostat equipped with a high sensitivity current follower to measure nanopipette probe currents with a bandwidth of 10 kHz for the current range measured herein. The SICM setup was controlled through a field-programmable gate array (FPGA) card (PCIe-7852R, National Instruments) using a home-written program in a LabView interface.

Numerical simulations

The simulation model was built in the Comsol Multiphysics (version 4.4) software package using geometrical parameters of the pipette probes available from TEM data. Numerical resolution of the system of governing differential equations was achieved in a two-dimensional axisymmetric formulation for computational efficiency. The mesh size was refined down to 4 nm resulting in about 140000 triangular mesh elements. For more details of the numerical modeling see Supporting Information SI-1.

RESULTS AND DISCUSSION

Operational principles

Electrochemical and chemical processes in electrolyte solutions involve a change of the charge state of species near the electrode/electrolyte interface. The change of the charge number and concentration of the different ions results in a corresponding change of electrophoretic mobility, which can be considerable for cases where there is a conversion of neutral molecules into a set of ionic species (*e.g.* hydrazine oxidation, $N_2H_4 - 4e^- \rightarrow N_2 + 4H^+$) or transformation of ions into uncharged undissociated compounds takes place (for instance, the hydrogen evolution reaction, $2H^+ + 2e^- \rightarrow H_2$). Since the conductivity of an electrolyte is determined by the overall concentration and mobility of the charge carriers present in the medium, a local heterogeneous reaction of this type will produce a spatial redistribution of ions near the reactive site, resulting in a variation of conductance within the diffusion layer (concentration-boundary layer near the electrode). The chemical transformation therefore leads to an increase or decrease of electrolyte conductivity and this effect can become detectable with a reasonable amount of redox molecules (with respect to electrolyte concentration). As we demonstrate below, these variations of local ionic conductance within a concentration-boundary layer near electrodes can be successfully

accessed with a scanning nanopipette in the SICM configuration and, hence, this opens up the possibility to employ ion conductance probes for imaging electrode (interfacial) reactivity.

Figure 1a schematically illustrates the working principle of SICM for these functional measurements. Similar to a classical SICM setup, ion current is driven through the pipette tip by the bias, ΔV, applied between the QRCE in the pipette (which is at ground) and that in the solution bulk. This allows accurate vertical tip positioning by using the AC feedback induced by tip oscillation[40,41] (amplitude, Δz, as illustrated on Figure 1) or by bias modulation[19] and the detection of local changes in ionic conductance through the direct current (DC), measured at the current follower A_1. The rate of the electrochemical reaction at the substrate electrode is controlled by the potential value, $E_{sub}+\Delta V$, with respect ground, or E_{sub} *vs* QRCE in the solution bulk. In this case, the current flowing through the current follower A_2 is the sum of the conductance current at A_1 and the faradaic current due to electrochemical oxidation/reduction at the working (substrate) electrode. This electrical configuration requires that the active area of the substrate electrode is small in comparison with the QRCEs in order to keep the conductance current induced by the potential difference between the substrate and the tip at a minimum (see details in Supporting Information SI-2). If this condition is satisfied, then the nanopipette can be used to probe dynamic processes at electrodes, as exemplified herein during voltammetric measurements, where the substrate potential is scanned over a wide range and the corresponding conductance current is measured simultaneously at every image pixel. This configuration is particularly advantageous for imaging, as it does not overcomplicate the experimental setup and it brings more versatility compared to other modifications of SICM instrumentation for ion flux imaging.[43]

Another important aspect for accurate measurements with SICM is the performance characteristics of the pipette probe, determined by its geometrical parameters. Both the lateral resolution and current sensitivity depend on the mass transport of ions through the nanopipette, which requires precise characterization of the probe (opening size, inner/outer cone angle and glass wall thickness) for quantitative measurements.[44,45] Figures 1b and c show electron micrographs of typical nanopipette probes. As can be seen, pipettes can be reasonably well approximated with a truncated cone shape with opening radii of ~100 and ~200 nm, and almost constant semi-angle (3.5°/5.5° and 4.2°/ 6.7°, inner/outer wall, respectively). This level of detail is important for quantitative data analysis, which can be achieved using simulation tools to treat mass transport and ion conductivity (*vide infra*).

Measurements near active reaction sites

The magnitude of ionic fluxes near reactive sites at interfaces (within the concentration-boundary layer) depends on the type of species involved, reaction stoichiometry and the rate. To exemplify this concept, it is convenient to consider the one-electron transfer that results in the transformation of a neutral redox molecule into an ionic compound, such as ferrocene methanol (Fc) oxidation ($Fc - e^- \rightarrow Fc^+$), taking place at a mass transport-limited rate at 25 μm disk Au UME. Electroneutrality requires supporting electrolyte ions to counterbalance the charge of Fc^+ in the diffusion layer by repulsion of f moles of cations and attraction of (1-f) moles of anions for each generated mole of ferrocenium methanol, as illustrated in Figure 2a. The conductivity at every location of the solution is therefore the sum of charge carrier concentrations, c_i, multiplied by their respective mobilities u_i and charge numbers z_i. Taking into account the electroneutrality condition as discussed above, the conductivity σ can be expressed using the local concentration of generated Fc^+:

$$\sigma = F\sum_i |z_i| c_i u_i = F(c_{Fc+}u_{Fc+} + c_{K+}u_{K+} + c_{NO3-}u_{NO3-}) =$$
$$= F[c_{Fc+}u_{Fc+} + (c^0_{salt} - fc_{Fc+})u_{K+} + (c^0_{salt} + (1-f)c_{Fc+})u_{NO3-}] \quad (1)$$

Herein, f is a factor that determines the local ionic composition within the diffusion layer: for f = 0.5 the supporting electrolyte salt (present in solution bulk and in the nanopipette at a concentration c^0_{salt}) balances the generated charge with equivalent cation and anion contributions, while f = 1 denotes substitution of electrolyte cations by Fc^+. The resulting change in local conductivity is thus dependent on the relative amount of species with different electrophoretic mobility (*e.g*, Fc^+) with respect to the local concentrations of supporting electrolyte ions (K^+ and NO_3^-). Similar considerations can be applied for heterogeneous reactions involving anionic species (*e.g.* ferro/ferricyanide) with electroneutrality maintained by counterbalancing of the local charge through redistribution of the supporting electrolyte salt.

To probe the resulting conductive properties of the concentration-boundary layer, a series of approaches (over an Au UME held at -0.2 V vs bulk QRCE, no Fc oxidation) and retracts (for which the substrate potential was switched to 0.2 V to drive the diffusion-limited oxidation of Fc into Fc^+) was performed using ~175 nm radius nanopipette tip. A relatively large nanopipette probe was chosen to avoid any possible additional complications from ion current rectification phenomena[29] to the mass transport through the nanopipette, which can affect both steady-state[28] and transient[46,47] measurements, although such effects could be accounted for in the future. As seen from Figures 2b and c, an electrochemical reaction at the substrate UME evidently changes the SICM approach curve. Moreover, the contrast between an active and inert substrate is dependent on the polarity of the SICM tip: at negative SICM tip bias there is a noticeable change in conductance across the diffusion layer adjacent to the active electrode (smaller conductance current), while at the opposite (positive) polarity any difference between the inert and active

substrate is hardly distinguishable, *i.e.* the measured current-distance approach curves over active and inert electrode are closely similar. Note the difference in the normalized current scale on the plots in Figures 2b and c.

To account for this result, a finite element method model was built, taking into consideration the geometrical characteristics of the tip, the substrate, their relative positions, electrolyte properties, and ionic composition of the concentration-boundary layer (see Supporting Information SI-1 for more details). Fitting of the experimental data with the simulation has f as the only adjustable parameter. The best fit was achieved with essentially equivalent substitution of supporting electrolyte cations by the generated Fc^+ (f = 0.925). This value of f provided good agreement with data at both tip polarities as evident from Figures 2b and c. The value of f close to 1 indicates a fundamental condition for electrolytes, highlighting that apart from electroneutrality, the ionic strength is also maintained across the medium. Ferrocenium ions, which replace almost equivalent amounts of K^+ from the electrolyte, have *ca.* 65% smaller ionic mobility, resulting in noticeable change in the conductive properties of the diffusion layer at the UME, and, more importantly, inside the negatively biased nanopipette tip. Because the nanopipette resistance is the key factor that dominates the ion current at a broad range of probe-to-substrate distances, even a relatively small variation of conductivity within the probe (especially at the tip) leads to a significant change of the overall measured ionic conductance.

Importantly, the strategy adopted, in which the AC component due to tip oscillation was used for positioning, is further advantageous for avoiding the convolution of topographical information with the measurement of local reactivity. The magnitude of the AC current is simply the gradient of the DC current-distance relationship at a particular distance. Figure 2d compares

experimental and simulated AC ion current amplitude values as a function of tip-substrate separation. The AC components of the nanopipette ion current are most sensitive to the probe proximity to the substrate, where steep changes of tip-to-substrate gap resistance occur, rather than changes of local conductivity, and can therefore be used for reliable probe positioning. As shown on Figure 2d, this is well evidenced by the theoretical results and experimental observations, which are all in close agreement, regardless of the substrate activity.

Computed conductivity maps (Figure 2e and f) evidence the importance of the probe polarity, which determines the sensitivity of the nanopipette towards the ion flux of generated Fc^+. At negative tip bias, electrogenerated Fc^+ travels into the nanopipette and accumulates at the tip, leading to the substitution of the more mobile charge carriers, K^+, by "slow" Fc^+, and a subsequent increase of the overall resistance. In contrast, at positive tip bias, the imposed electric field at the tip leads to the rejection of Fc^+ cations from entering the probe, and the ionic composition (and conductivity) of the nanopipette remains almost unaffected (as illustrated on Figure 2f), resulting in a very small change of the mass flux through the nanopipette due to the generation of charged species at the UME. This result highlights a further possible means of separating topography and interfacial reactivity in SICM, simply by switching the tip polarity.

Dynamic Voltammetric Imaging

Figure 3a demonstrates the application of SICM for dynamic visualization of interfacial reactivity, *i.e.* with a pipette probe (held at constant bias) sensing conductance variations during voltammetric measurement at the substrate. In this example, a ~200 nm radius pipette probe biased at -0.25 V was scanned over a *ca.* 1.2 μm diameter Pt UME, where the electrochemical reduction of protons and oxidation of hydrazine could take place (depending on the applied potential). At every scan pixel, the probe approached the substrate held at -0.2 V with respect to

QRCE in bulk solution (to ensure that no significant reactions took place) and as the positionable feedback set point was triggered (AC amplitude threshold), a voltammogram (between potential limits of -1.2 V and 0.75 V) was recorded at the substrate. The resulting data (45 by 45 probe locations, resolved with a 125 nm pitch) comprised a set of lateral and vertical tip positions (sample topography) along with a sequence of 380 substrate and tip current values measured during voltammetric sweep at each probe position (at 2025 locations).

The recorded topographical image (Figure 3b) evidences some substrate tilt, although thermal drift may also contribute to the image.[42] The important point is that the tip can successfully locate the near interface at a large array of positions. Figure 3c exemplifies one of the voltammetric responses (from both the electrode and the pipette tip recorded simultaneously), acquired over the central part of the Pt UME during imaging. As shown, the nanopipette probe successfully detects changes of ion conductance, caused by consumption of aqueous protons (conductivity decrease) due to electroreduction of hydronium ions in the potential range -0.95 V to -1.2 V, and the release of four H^+ per single hydrazine molecule due to its oxidation at more positive potentials (0.1 V – 0.75 V), which causes an increase of conductivity and tip current. The probe and substrate currents are well-correlated in the reduction part of I-V curve, where the hydrogen evolution reaction occurs. Hydrazine electrooxidation on Pt electrodes (and especially in the presence of H_2SO_4) is a more complex process[48] in which potential-dependent oxide formation occurs on the electrode surface, leading to a large hysteresis between the forward and reverse voltammetric scans and a rather unusual shape,[49] including a loop (crossing point) on the cathodic and anodic going scans. The corresponding conductance measurements in the diffusion layer demonstrate a typical mass transport-limited plateau. While broadly tracing the voltammetric wave, there is some hysteresis between the substrate voltammogram and tip

response on the reverse voltammetric scan that suggests this type of measurement could be mechanistically revealing.

Voltammograms recorded at scan pixels can be conveniently represented as a sequence of images, resolved at a set of discrete substrate potentials. Figure 3d shows a few frames (see the full sequence of 380 images in the video file Movie1.qt in Supporting Information), illustrating spatially resolved maps of electrochemical activity. The images demonstrate clear contrast between active (Pt surface) and inert (glass) regions, with the diffuse nature of the active region due to the diffusion of reagents and products. Importantly, because of the procedure adopted, there is no influence from topographical effects, with the image purely representing a reaction-diffusion map. Note that the data shown are neither interpolated nor filtered.

It is further important to note that the recorded images do not evidence noticeable influence from the scanning probe on mass transport at the substrate, which can be an issue for many scanning probe techniques, even with relatively small probes. The geometrical arrangement of probes for SECM (micro- or nanoelectrodes with a large glass sheath) or even conical AFM tips often leads to a partial blockage of the diffusion layer at the substrate and therefore results in some perturbation of the measurement.[50,51] This is not much of an issue for SICM (highly slender probes) as even the presence of a relatively large (~200 nm radius) nanopipette above ~600 nm radius active electrode area has minor influence on the overall substrate electrode current. This is evident from Figures 4a and b, which compare maps of the tip and UME currents, respectively, as a function of tip position extracted from the image sequence, at a substrate potential of 0.75 V (mass transport-limited hydrazine oxidation). As can be seen, the substrate current as a function of tip position is relatively uniform, with just a slightly smaller current, seen when the nanopipette probe is above the active area of the Pt disk. The current

profiles shown on Figure 4c, extracted from potential-dependent substrate current images (as a function of tip position), indicate that the current drop at the substrate is (at most) about 500 pA, which corresponds to only about ~ 5% of redox mediator flux at the microelectrode, in good agreement with numerical simulations (see Supporting Information SI-3). This is a relatively small perturbation, comparable to the blocking effect of optimal AFM tips.[51]

High-Speed Imaging

While the dynamic imaging described is a very robust approach for studying various electrochemical systems, imaging at high tip scanning rates can offer numerous advantages, from the capability of acquiring a large amount of information (of extended sample areas) to the avoidance of limitations from long imaging times, such as chemical and physical changes to the substrate during the scanning, sample ageing, probe fouling, solvent evaporation, and the instability of electrolyte solutions. As we showed recently,[52] high-speed imaging for SEPMs requires a set of factors to be carefully considered for successful application with a particular technique, including the constraints of the piezoelectric positioners for probe translation, the rate of positional feedback, the characteristic probe response time and the bandwidth of current amplifiers. Most of the imaging limitations can be overcome using a harmonic scan pattern (such as an Archimedes spiral as exemplified herein) for smooth probe translation and a trace/retrace protocol, where a probe is scanned close to the substrate to acquire its topography at a relatively slow scan rate followed by a series of quick retraces over the set of acquired topographical coordinates (x, y and z). As we show herein, this strategy can be applied to the SICM technique for high-speed imaging of electrochemical activity at interfaces.

Figure 5a demonstrates a prescan image (acquisition time 390 s) for the electrochemical oxidation of $FcTMA^+$ at a Pt electrode (~430 nm radius disk) at 0.4 V recorded at 5.2 μm s^{-1}

translation rate with a 95 nm radius nanopipette probe (biased at -0.25 V). The original image contained about 1.52×10^6 pixels, which were smoothed by averaging down to 38091 data points on the presented image, resulting in a pixel density of 162 pixels μm^{-2}. As can be seen, the reaction zone at the UME is clearly resolved, with the lowest probe currents observed above the active region (Pt surface). Similarly to ferrocene methanol oxidation, the generation of $FcTMA^{2+}$ results in a decrease of ionic conductance at the nanopipette tip due to repulsion of the supporting electrolyte cations (K^+, which has 30% higher ionic mobility than $FcTMA^{2+}$) from the diffusion field.

Following acquisition of the substrate topography, a series of 202 high-speed frames (101 forward and reverse) was collected with a probe operating at a speed 180 $\mu m\ s^{-1}$. Each image frame has been resolved at a constant substrate potential, which ranged from 0.4 V (mass transport-limited oxidation of $FcTMA^+$) to 0 V (no $FcTMA^{2+}$ generation) with a step of 4 mV between images. Figure 5b depicts six of the acquired images, constructed from both forward and reverse scans recorded at a rate of *ca.* 4.16 seconds per frame (scan area around 50 μm^2) with *ca.* 16250 pixels per image (see full image sequence as a video file Movie2.qt in Supporting Information). As illustrated by the image sequence, the nanopipette tip current contrast vanishes gradually with a decrease of electrode activity: as the $FcTMA^+$ oxidation process is switched off at the substrate UME, the less is the change of ionic composition near the active electrode area (compared to bulk).

Interestingly, convection does not seem to play a major role for imaging at such a high frame rate. As can be seen, for example by comparing the slow and fast images in Figures 5a and b at 0.4 V, scanning at elevated rates does not significantly compromise image quality. Figure 5c depicts the tip current profiles across the central part of the UME in cases of slow (preliminary

scan) and high-speed imaging and confirms a minor influence of probe translation on the measured ionic fluxes. As can be seen, there is little difference between the probe current profiles even for a 35-fold increase (from 5.2 to 180 μm s^{-1}) of the probe scanning rate.

Figure 5d demonstrates the current profiles across the image frames recorded at different substrate potentials. The magnitude of the current change between the active electrode and surrounding glass diminishes with a decrease of the reaction driving force (overpotential) and this is well evidenced from the current profiles and the resolved images. As can be seen, the sensitivity of the technique is high enough to detect variations of the local conductivity even at a very low overpotential (with the substrate biased at 4 mV vs QRCE in the bulk). The presented current profiles also suggest that the diameter of the active area of the substrate UME is around 0.7 – 0.8 μm, very close to the Pt disk size of ~860 nm (estimated from voltammetry), providing a good estimate of active region size even at a very large translation rate and regardless of the magnitude of the change in ionic compositions near the active site, as determined by the reaction rate at the electrode.

CONCLUSIONS

Scanning ion conductance microscopy has been shown to be a powerful technique for imaging electrochemical reactivity at interfaces. The magnitude of the ionic current flowing through the nanopipette probe is very sensitive to the local conductivity changes that occur near active sites and can be used for probing the spatial distribution of ion fluxes, arising due to (electro)chemical transformations. Along with the high resolving power intrinsic to SICM, the technique brings several important advantages over other electrochemical imaging methods, thanks to the simple protocols for probe fabrication, the possibility of simultaneous tracking of topography and reactivity, easily tuneable probe size and a small extent of perturbation exerted on the mass

fluxes at the substrate. Moreover, ion current measurements can be made with a high degree of accuracy. This makes SICM reactive imaging a very attractive alternative for the characterization of (electro)catalytic materials. At the same time, the possibility to translate the probe at very high scan rates (up to 1000 probe diameters per second) offers exciting opportunities for high-speed imaging with the frame rate approaching 4 s per snapshot with high pixel resolution.

A considerable issue in SEPM (particularly SECM) is the separation of topography and activity effects, and in this paper we have identified two simple approaches to easily resolve this problem. First, by using a distance-modulation SICM approach, we have shown that the resulting AC SICM current at the modulation frequency is relatively insensitive to reactivity of the surface, so that a combination of simultaneous AC and DC SICM measurements reveals both the substrate topography and the activity. Second, the potential applied to the SICM probe can be selected so that the DC probe response is sensitive to either the topography or activity. These deductions were aided by detailed finite element method modeling that allowed a thorough assessment and analysis of ion fluxes with the SICM reactive imaging technique.

REFERENCES

(1) Hansma, P. K.; Drake, B.; Marti, O.; Gould, S. A.; Prater, C. B. *Science* **1989**, *243*, 641-3.
(2) Korchev, Y. E.; Milovanovic, M.; Bashford, C. L.; Bennett, D. C.; Sviderskaya, E. V.; Vodyanoy, I.; Lab, M. J. *J. Microsc.* **1997**, *188*, 17-23.
(3) Happel, P.; Hoffmann, G.; Mann, S. A.; Dietzel, I. D. *J. Microsc.* **2003**, *212*, 144-151.
(4) Takahashi, Y.; Murakami, Y.; Nagamine, K.; Shiku, H.; Aoyagi, S.; Yasukawa, T.; Kanzaki, M.; Matsue, T. *Phys. Chem. Chem. Phys.* **2010**, *12*, 10012-7.
(5) Rheinlaender, J.; Schaffer, T. E. *Soft Matter* **2013**, *9*, 3230-3236.
(6) Gorelik, J.; Shevchuk, A. I.; Frolenkov, G. I.; Diakonov, I. A.; Lab, M. J.; Kros, C. J.; Richardson, G. P.; Vodyanoy, I.; Edwards, C. R.; Klenerman, D.; Korchev, Y. E. *Proc. Natl. Acad. Sci. U. S. A.* **2003**, *100*, 5819-22.
(7) Shevchuk, A. I.; Frolenkov, G. I.; Sanchez, D.; James, P. S.; Freedman, N.; Lab, M. J.; Jones, R.; Klenerman, D.; Korchev, Y. E. *Angew. Chem., Int. Ed. Engl.* **2006**, *45*, 2212-6.
(8) O'Connell, M. A.; Lewis, J. R.; Wain, A. J. *Chem. Commun.* **2015**, *51*, 10314-10317.
(9) Takahashi, Y.; Shevchuk, A. I.; Novak, P.; Murakami, Y.; Shiku, H.; Korchev, Y. E.; Matsue, T. *J. Am. Chem. Soc.* **2010**, *132*, 10118-10126.
(10) Takahashi, Y.; Shevchuk, A. I.; Novak, P.; Zhang, Y. J.; Ebejer, N.; Macpherson, J. V.; Unwin, P. R.; Pollard, A. J.; Roy, D.; Clifford, C. A.; Shiku, H.; Matsue, T.; Klenerman, D.; Korchev, Y. E. *Angew. Chem., Int. Ed.* **2011**, *50*, 9638-9642.
(11) Comstock, D. J.; Elam, J. W.; Pellin, M. J.; Hersam, M. C. *Anal. Chem.* **2010**, *82*, 1270-1276.
(12) Korchev, Y. E.; Raval, M.; Lab, M. J.; Gorelik, J.; Edwards, C. R.; Rayment, T.; Klenerman, D. *Biophys. J.* **2000**, *78*, 2675-9.
(13) Gorelik, J.; Shevchuk, A.; Ramalho, M.; Elliott, M.; Lei, C.; Higgins, C. F.; Lab, M. J.; Klenerman, D.; Krauzewicz, N.; Korchev, Y. *Proc. Natl. Acad. Sci. U. S. A.* **2002**, *99*, 16018-23.
(14) Nadappuram, B. P.; McKelvey, K.; Byers, J. C.; Güell, A. G.; Colburn, A. W.; Lazenby, R. A.; Unwin, P. R. *Anal. Chem.* **2015**, *87*, 3566-3573.
(15) Aaronson, B. D. B.; Güell, A. G.; McKelvey, K.; Momotenko, D.; Unwin, P. R. In *Nanoelectrochemistry*, Mirkin, M. V.; Amemiya, S., Eds.; CRC Press, 2015, pp 655-694.
(16) Wang, Y.; Kececi, K.; Velmurugan, J.; Mirkin, M. V. *Chem. Sci.* **2013**, *4*, 3606-3616.
(17) Williams, C. G.; Edwards, M. A.; Colley, A. L.; Macpherson, J. V.; Unwin, P. R. *Anal. Chem.* **2009**, *81*, 2486-2495.
(18) Takahashi, Y.; Kumatani, A.; Munakata, H.; Inomata, H.; Ito, K.; Ino, K.; Shiku, H.; Unwin, P. R.; Korchev, Y. E.; Kanamura, K.; Matsue, T. *Nat Commun* **2014**, *5*.
(19) McKelvey, K.; Perry, D.; Byers, J. C.; Colburn, A. W.; Unwin, P. R. *Anal. Chem.* **2014**, *86*, 3639-3646.
(20) McKelvey, K.; Kinnear, S. L.; Perry, D.; Momotenko, D.; Unwin, P. R. *J. Am. Chem. Soc.* **2014**, *136*, 13735-13744.
(21) Perry, D.; Al Botros, R.; Momotenko, D.; Kinnear, S. L.; Unwin, P. R. *ACS Nano* **2015**, *9*, 7266-7276.
(22) Chen, C.-C.; Zhou, Y.; Baker, L. A. *Annu. Rev. Anal. Chem.* **2012**, *5*, 207-228.
(23) Proksch, R.; Lal, R.; Hansma, P. K.; Morse, D.; Stucky, G. *Biophys. J.* **1996**, *71*, 2155-7.
(24) Morris, C. A.; Chen, C.-C.; Baker, L. A. *Analyst* **2012**, *137*, 2933-2938.
(25) Chen, C.-C.; Derylo, M. A.; Baker, L. A. *Anal. Chem.* **2009**, *81*, 4742-4751.
(26) Zhou, Y.; Chen, C.-C.; Baker, L. A. *Anal. Chem.* **2012**, *84*, 3003-3009.

(27) Prater, C. B.; Hansma, P. K.; Tortonese, M.; Quate, C. F. *Rev. Sci. Instrum.* **1991**, *62*, 2634-2638.
(28) Momotenko, D.; Cortes-Salazar, F.; Josserand, J.; Liu, S. J.; Shao, Y. H.; Girault, H. H. *Phys. Chem. Chem. Phys.* **2011**, *13*, 5430-5440.
(29) Wei, C.; Bard, A. J.; Feldberg, S. W. *Anal. Chem.* **1997**, *69*, 4627-4633.
(30) Sa, N.; Baker, L. A. *J. Am. Chem. Soc.* **2011**, *133*, 10398-10401.
(31) Sa, N.; Lan, W.-J.; Shi, W.; Baker, L. A. *ACS Nano* **2013**, *7*, 11272-11282.
(32) Bard, A. J. In *Scanning Electrochemical Microscopy, Second Edition*; CRC Press, 2012, pp 1-14.
(33) O'Connell, M. A.; Wain, A. J. *Anal. Chem.* **2014**, *86*, 12100-12107.
(34) Ludwig, M.; Kranz, C.; Schuhmann, W.; Gaub, H. E. *Rev. Sci. Instrum.* **1995**, *66*, 2857-2860.
(35) Macpherson, J. V.; Unwin, P. R. *Anal. Chem.* **2000**, *72*, 276-285.
(36) Kranz, C.; Friedbacher, G.; Mizaikofft, B.; Lugstein, A.; Smoliner, J.; Bertagnolli, E. *Anal. Chem.* **2001**, *73*, 2491-2500.
(37) McKelvey, K.; Edwards, M. A.; Unwin, P. R. *Anal. Chem.* **2010**, *82*, 6334-6337.
(38) Nioradze, N.; Chen, R.; Kim, J.; Shen, M.; Santhosh, P.; Amemiya, S. *Anal. Chem.* **2013**, *85*, 6198-6202.
(39) Szentirmay, M. N.; Martin, C. R. *Anal. Chem.* **1984**, *56*, 1898-1902.
(40) Shevchuk, A. I.; Gorelik, J.; Harding, S. E.; Lab, M. J.; Klenerman, D.; Korchev, Y. E. *Biophys. J.* **2001**, *81*, 1759-1764.
(41) Li, C.; Johnson, N.; Ostanin, V.; Shevchuk, A.; Ying, L.; Korchev, Y.; Klenerman, D. *Prog. Nat. Sci.* **2008**, *18*, 671-677.
(42) Kim, J.; Shen, M.; Nioradze, N.; Amemiya, S. *Anal. Chem.* **2012**, *84*, 3489-3492.
(43) Laslau, C.; Williams, D. E.; Wright, B. E.; Travas-Sejdic, J. *J. Am. Chem. Soc.* **2011**, *133*, 5748-5751.
(44) Edwards, M. A.; Williams, C. G.; Whitworth, A. L.; Unwin, P. R. *Anal. Chem.* **2009**, *81*, 4482-4492.
(45) Weber, A. E.; Baker, L. A. *J. Electrochem. Soc.* **2014**, *161*, H924-H929.
(46) Guerrette, J. P.; Zhang, B. *J. Am. Chem. Soc.* **2010**, *132*, 17088-17091.
(47) Momotenko, D.; Girault, H. H. *J. Am. Chem. Soc.* **2011**, *133*, 14496-14499.
(48) Chen, C.-H.; Jacobse, L.; McKelvey, K.; Lai, S. C. S.; Koper, M. T. M.; Unwin, P. R. *Anal. Chem.* **2015**, *87*, 5782-5789.
(49) Aldous, L.; Compton, R. G. *Phys. Chem. Chem. Phys.* **2011**, *13*, 5279-5287.
(50) Wittstock, G.; Burchardt, M.; Pust, S. E.; Shen, Y.; Zhao, C. *Angew. Chem., Int. Ed.* **2007**, *46*, 1584-1617.
(51) Burt, D. P.; Wilson, N. R.; Janus, U.; Macpherson, J. V.; Unwin, P. R. *Langmuir* **2008**, *24*, 12867-12876.
(52) Momotenko, D.; Byers, J. C.; McKelvey, K.; Kang, M.; Unwin, P. R. *ACS Nano* **2015**, *9*, 8942-8952.

ACKNOWLEDGMENT

This work was supported by the European Research Council through Project ERC-2009 AdG 247143-QUANTIF and a Marie Curie IntraEuropean Fellowship 626158 FUNICIS (D.M.). The authors also acknowledge Ms. Sophie L. Kinnear for her kind help with software development, Dr. Robert A. Lazenby for fruitful discussions about experimental setup and Dr. Alex Colburn for high-speed current amplifiers.

ASSOCIATED CONTENT

Supporting Information. Numerical simulations of the nanopipette measurements, description of electrical setup configuration and relative substrate size, the effect of nanopipette on measured substrate currents, two video files constructed from image sequences, depicting maps of electrochemical activity as a function of the applied substrate potential. This material is available free of charge via the Internet at http://pubs.acs.org.

COMPETING FINANCIAL INTERESTS

The authors declare no competing financial interests.

FIGURES

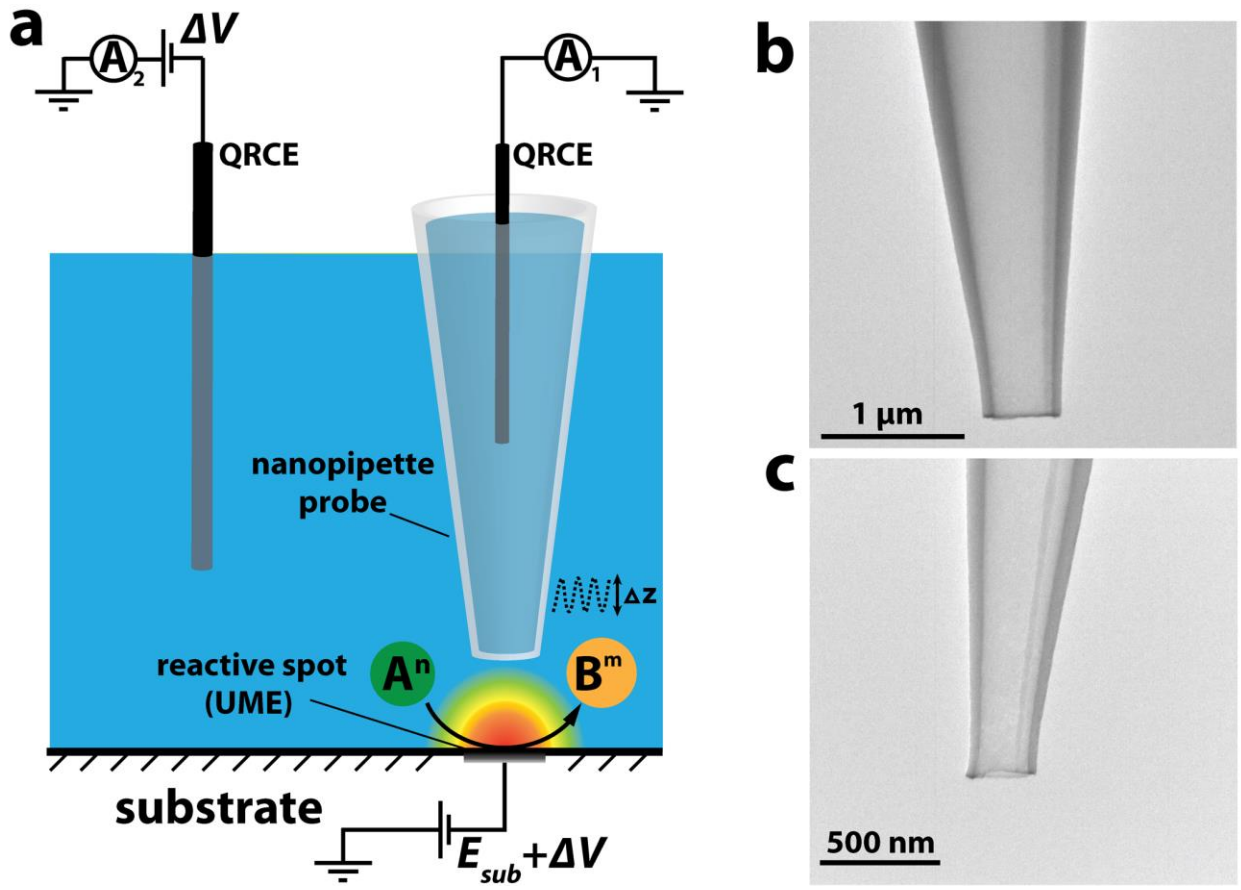

Figure 1. a) Schematic representation of the experimental setup for reaction mapping with SICM. b), c) TEM images of nanopipette probes of ~200 nm and ~100 nm opening radius, respectively.

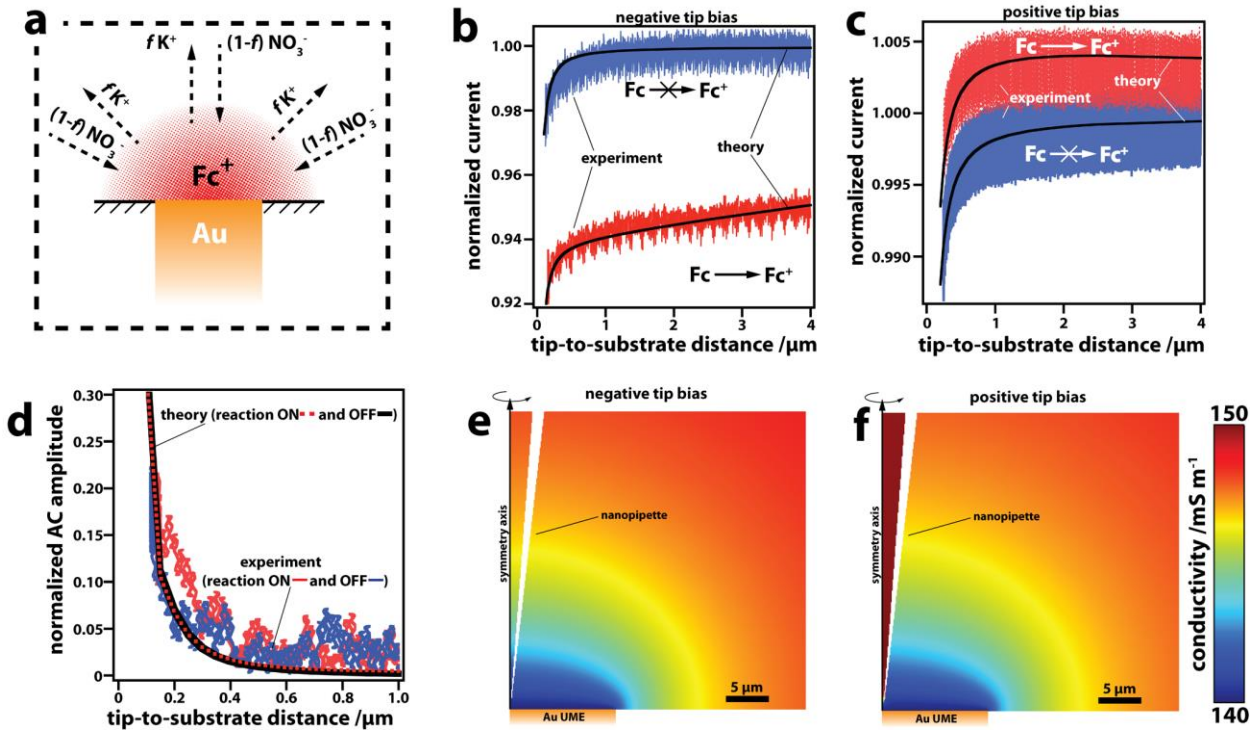

Figure 2. Probing the diffusion (concentration-boundary) layer with a nanopipette. a) Schematic representation of the ion redistribution at the diffusion layer of generated Fc^+ adjacent to an Au UME. b), c) Experimental (red and blue traces) and simulated (solid black lines) SICM current-distance curves acquired with a nanopipette (biased at -0.1 and +0.1 V, respectively) positioned over an inert (blue) and Fc^+ generating (diffusion-controlled rate) 12.5 μm radius Au UME (red). Experimental conditions (1.95 mM and 1.45 mM Fc for (b) and (c), with 10 mM KNO_3 in bulk solution, and nanopipettes of 175 nm opening radii as determined by TEM) were mimicked in the simulation with the best fit with an *f* parameter of 0.925. d) Experimental (red, reaction on, and blue, reaction off) and theoretical (black and red dashed lines) AC amplitude – distance relationships for a nanopipette positioned over an inert and Fc^+ generating UME. Note that the theoretical curves with the electrode on and off essentially coincide. e), f) Simulated conductivity

distributions (magnified view) with a nanopipette (biased at ±0.1 V) positioned at 1 μm distance from an Fc^+ generating substrate electrode (Au UME).

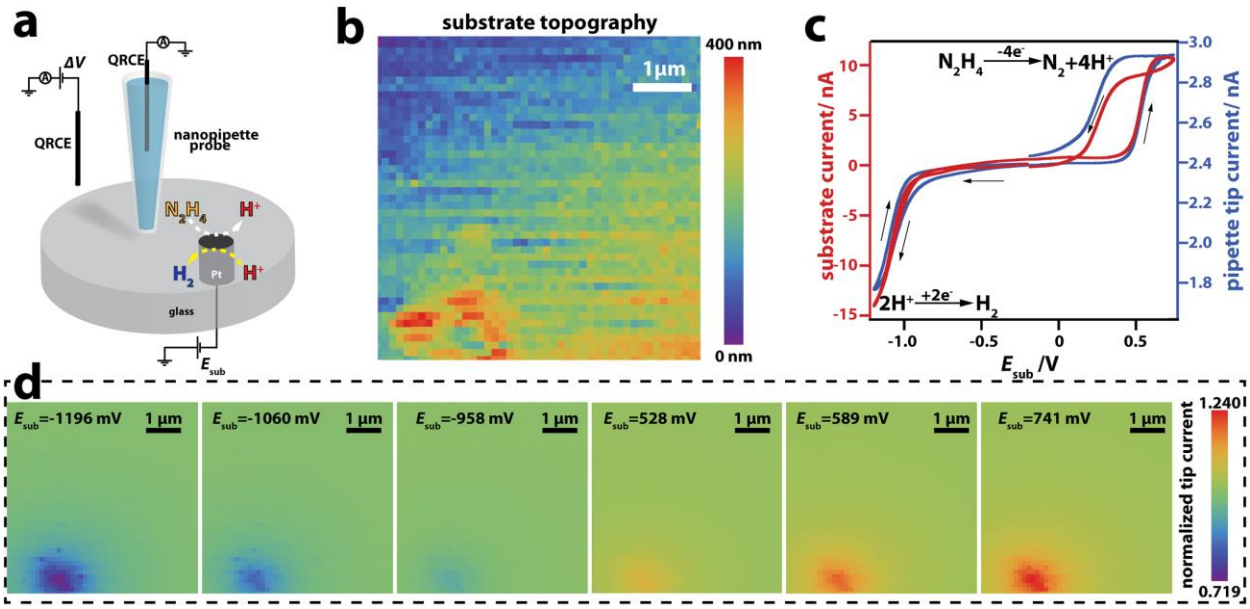

Figure 3. Dynamic reaction imaging with SICM. a) Schematic representation of the experimental setup employed for mapping hydrazine oxidation and proton reduction at ~600 nm radius Pt UME. b) Topography map (45 by 45 pixels, 125 nm step size) during a hopping scan. The nanopipette, biased at -0.25 V, was approached to the substrate (held at -0.2 V vs Ag/AgCl QRCE in bulk) at every pixel at a speed of 250 nm s^{-1} and then retracted by 1 μm before being repositioned above the next location. c) Substrate (red) and nanopipette probe (blue) voltammograms acquired with the nanopipette at the central part of the substrate electrode during the potential sweep at the Pt UME (-1.2 V to 0.75 V) at a scan rate 0.5 V s^{-1}. The electrolyte solution contained hydrazine sulphate $N_2H_4 \cdot H_2SO_4$ and KNO_3 at 20.5 mM and 10 mM, respectively. The arrows on the graph indicate the direction of the potential sweep. d) Electrochemical images (6 frames) from a 380-snapshot image sequence, constructed from a voltammetric data resolved at each image pixel (see full image sequence in the form of a video file Movie1.qt in Supporting Information). The nanopipette current has been normalized by the

value at the point of the closest approach (at each individual pixel) with the substrate potential held at -0.2 V.

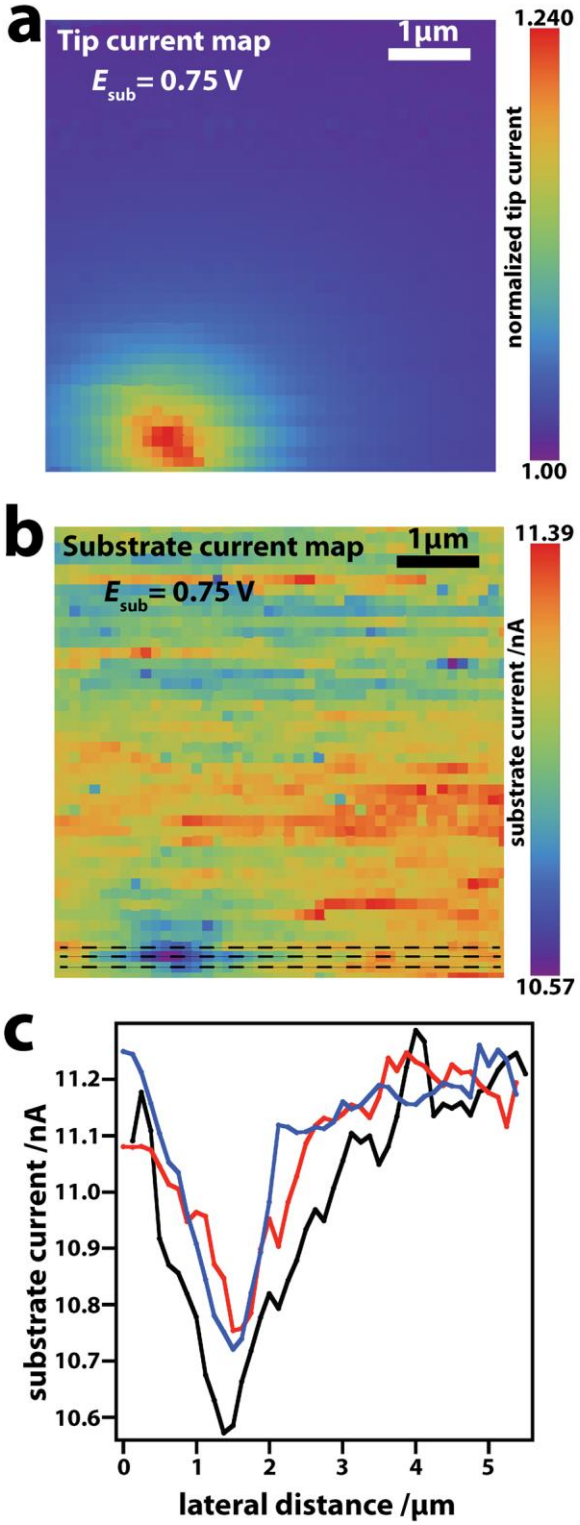

Figure 4. The effect of a nanopipette tip on the mass-transport at the substrate. Maps of a) normalized tip current and b) corresponding map of substrate current as a function of nanopipette

position at 0.75 V (mass transport-limited hydrazine oxidation. c) Substrate current profiles extracted from substrate current map at positions indicated by dashed lines in b).

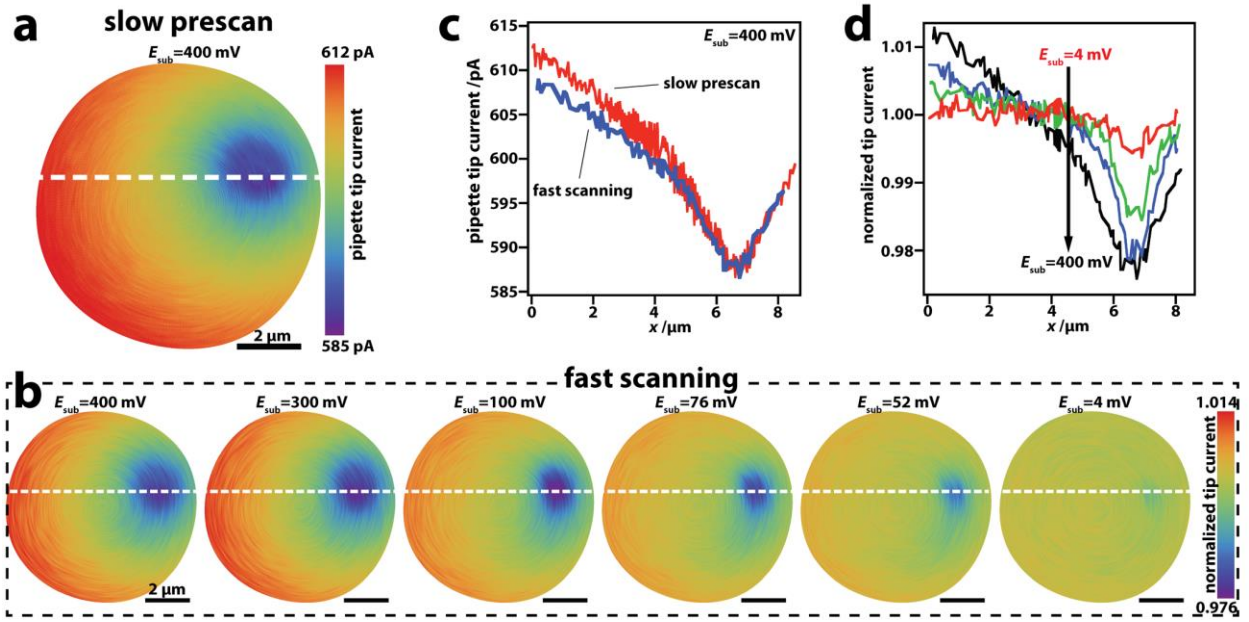

Figure 5. a) High-speed electrochemical imaging of reactions with SICM. a) Electrochemical image of ~430 nm radius Pt UME (held at 0.4 V) recorded with a ~95 nm radius nanopipette biased at -0.25 V *vs* QRCE in bulk solution during a topographical prescan at 5.2 µm s^{-1} in electrolyte solution containing 2 mM $FcTMA^+$ (diffusion-limited oxidation) and 10 mM KNO_3. b) A set of high speed images constructed from both forward and reverse scans (for improved image quality) recorded at 180 µm s^{-1} probe translational speed at different substrate potentials (see the full frame sequence Movie2.qt in the form of a video file in Supporting Information). The probe currents are normalized with respect to the average ion current for every snapshot. c) Nanopipette current profiles (along the dashed white line on the images) depicting the comparison between high-speed (red) and slow prescan (blue) imaging of diffusion-controlled $FcTMA^+$ oxidation (substrate held at 0.4 V). d) Normalized tip current profiles, demonstrating the effect of the substrate potential on the normalized tip current. Red, green, blue and black lines correspond to substrate electrode potentials of 4, 52, 76 and 400 mV vs QRCE in solution bulk, respectively. White dashed line on a) and b) denotes the position of the current profiles

shown on c) and d). Scale bar 2 μm. Note, the current data was smoothened using Gaussian filter.

For TOC only

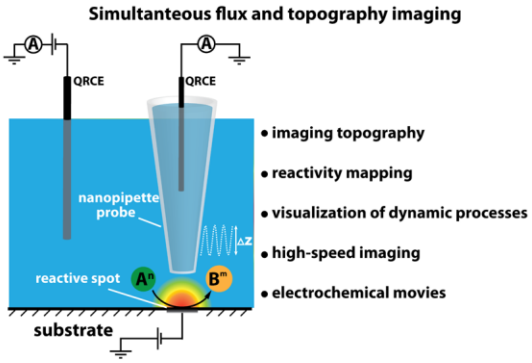
Simultanteous flux and topography imaging
QRCE
QRCE
nanopipette probe
ΔZ
reactive spot
substrate
• imaging topography
• reactivity mapping
• visualization of dynamic processes
• high-speed imaging
• electrochemical movies